Control of Fuel Cell Breathing

By Jay T. Pukrushpan, Anna G. Stefanopoulou, and Huei Peng

Avoid fuel cell oxygen starvation with air flow controllers.

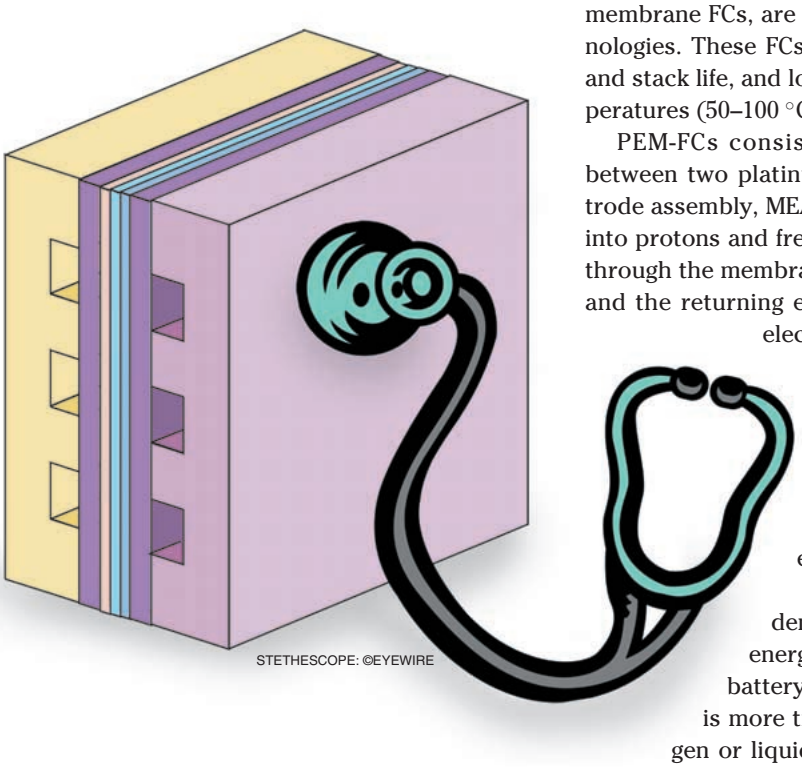

STETHESCOPE: ©EYEWIRE

Fuel cell systems offer clean and efficient energy production and are currently under intensive development by several manufacturers for both stationary and mobile applications. The fuel cell (FC) concept dates back to the early 1800s. The idea was first published in [1], and its invention has largely been attributed to W.R. Grove [2]. Although the availability and abundance of fossil fuel has limited interest in FCs as a power source [3], recent advances in membrane and electrode material, reduced usage of noble metal catalysts, efficient power electronics, and electric motors have sparked interest in direct electricity generation using FCs. In particular, proton exchange membrane FCs (PEM-FCs), also known as polymer electrolyte membrane FCs, are considered to be more developed than other FC technologies. These FCs have high power density, solid electrolyte, long cell and stack life, and low corrosion. Moreover, these FCs operate at low temperatures (50–100 °C), which enables fast start-up.

PEM-FCs consist of a proton-conducting membrane sandwiched between two platinum-impregnated porous electrodes (membrane electrode assembly, MEA), as shown in Figure 1. Hydrogen molecules are split into protons and free electrons at the anode catalyst. The protons diffuse through the membrane to the cathode and react with the supplied oxygen and the returning electrons to produce water. During this process, the electrons pass through an external load circuit and provide useful electric energy. A typical PEM-FC provides up to 0.6 W/cm^2 depending on the catalyst loading, the membrane and electrode material, and the reactant (oxygen O_2 and hydrogen H_2) concentration in the anode and cathode. To satisfy different power requirements, many FCs are connected electrically in series to form an FC stack (FCS).

Compared to batteries, FCs provide higher energy density. For example, a methanol FC powertrain has an energy density of about 1,900 Wh/kg, whereas a lead acid battery provides 40 Wh/kg [4]. Moreover, battery recharging is more time consuming than refueling FC vehicles with hydrogen or liquid fuel. FCs have higher efficiencies compared to heat engines, and their use for modular electricity generation and electric vehicles propulsion is promising [5]. FC efficiency is high at partial loads, which occur in the majority of urban and highway driving scenarios [6]. At the nominal driving speed of 30 mph, the efficiency of an FC electric

0272-1708/04/$20.00©2004IEEE

drive using hydrogen from natural gas is twice as high as that of a conventional internal combustion engine [4]. Using pure hydrogen as fuel can reduce vehicle emissions, especially in densely populated urban environments.

The dependence of PEM on high-purity hydrogen reactant requires novel hydrogen generation and storage technologies. Fuel processors that reform hydrocarbon fuel into gas rich in hydrogen are currently considered a near-term solution to the hydrogen generation problem [7]. Controlling fuel processors to provide hydrogen on demand can mitigate problems associated with hydrogen storage and distribution [8], [9]. In the long term, hydrogen generation by means of water electrolysis based on renewable energy from wind, waves, and sun, or reformed hydrocarbon fuel through biomass will help reduce the current dependence on fossil fuels.

The principle of electricity generation from a PEM-FC is straightforward when the correct material properties, cell structure, and hydrogen are in place. The FC power response, however, is limited by air flow, pressure regulation, heat, and water management [10]. Since current is instantaneously drawn from the load source connected to the FC, the FC control system is required to maintain optimal temperature, membrane hydration, and partial pressure of the reactants across the membrane to avoid detrimental degradation of the FC voltage, which can reduce efficiency. These critical FC parameters must be controlled over a wide range of current, and thus power, by a series of actuators such as valves, pumps, compressor motors, expander vanes, fan motors, humidifiers, and condensers. The resulting auxiliary actuator system, shown in Figure 2, is needed to make fine and fast adjustments to satisfy performance, safety, and reliability requirements that are independent of age and operating conditions. These requirements create challenging spatial and temporal control problems [11]. In this article we assume that compressed hydrogen is available, and we concentrate on the challenges associated with the temporal characteristics of the air (oxygen) supply. The overall FC system and relevant variables are shown in Figure 2.

We use control design techniques based on a dynamic model developed in [12] and [13]. A similar modeling

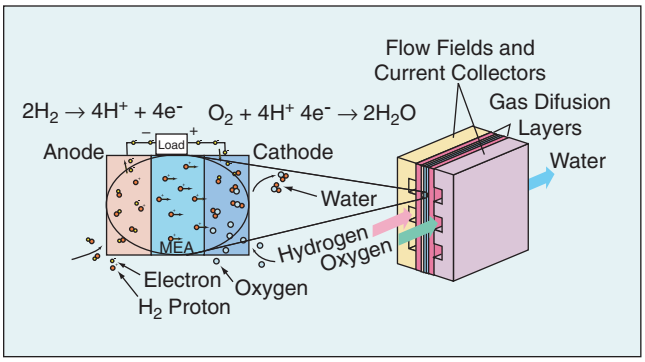

Figure 1. *PEM FC reactions and structure. Water, electrical energy, and heat arise through the combination of hydrogen and oxygen. Although the concept is simple, its implementation requires a complex structure, sophisticated materials, and accurately controlled conditions.*

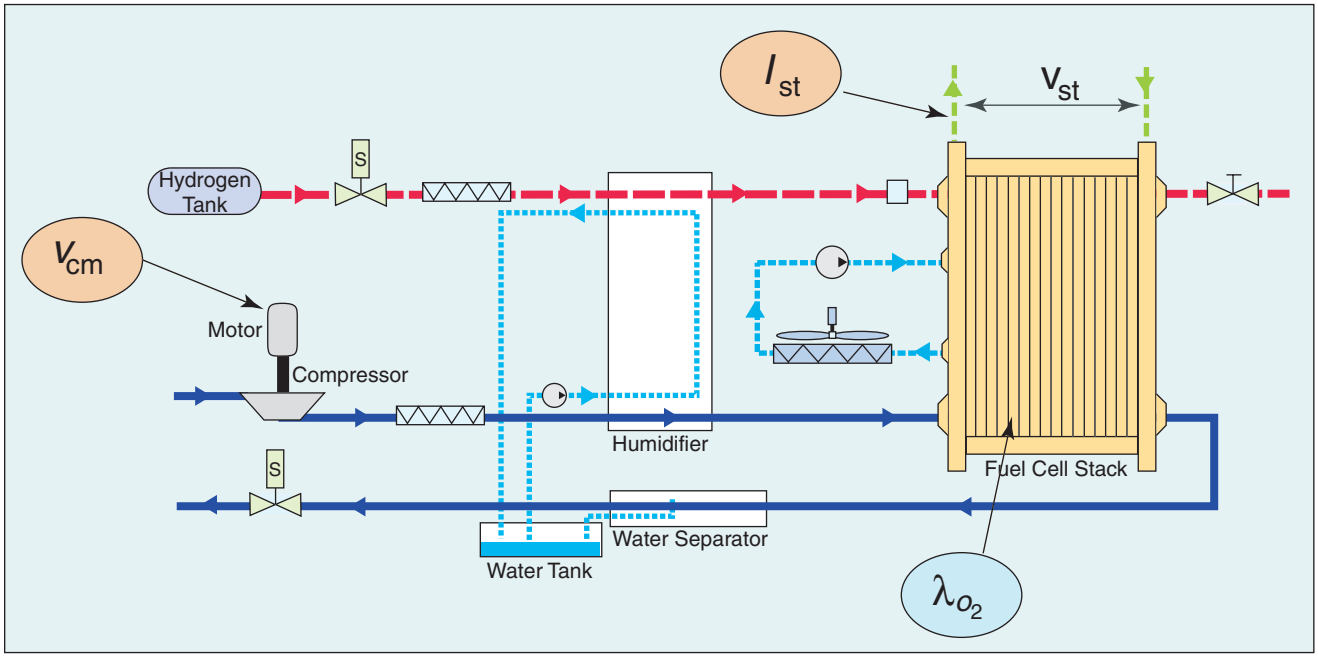

Figure 2. *FC system with major control subsystems. A fuel cell system includes four subsystems that manage the air, hydrogen, humidity, and stack temperature. The humidification and cooling are sometimes combined in one subsystem. The figure also shows the control inputs and outputs of the air subsystem.*

approach is presented in [14] and discussed in [15] and [16]. The stack terminal voltage V_{st} is calculated based on the dynamically evolving load current and FC operating conditions such as hydrogen and oxygen partial pressure. The physical parameters are calibrated based on data reported in the literature, and the system is sized to represent the high pressure FC stack used in the Ford P2000 Fuel Cell vehicle [10]. The model is then used to analyze and design an air flow controller for the FC stack supercharging device that provides fast and robust air flow to the cathode.

Simple control techniques provide useful insight critical for the development of robust and efficient fuel cell systems.

The FC air flow needs to be controlled rapidly and efficiently to avoid oxygen starvation and extend the life of the stack [11], while minimizing parasitic losses of the compressor [17]. Oxygen starvation is a complicated phenomenon that occurs when the partial pressure of oxygen falls below a critical level at any location within the meander of the air stream in the cathode [18]. This phenomenon entails a rapid decrease in cell voltage, which in severe cases can cause a hot spot, or even burn-through on the surface of a membrane. To prevent this catastrophic event, the stack diagnostic system must either remove the current from the stack or trigger shut-down. Although the oxygen starvation is spatially varying, this phenomenon is believed to be avoidable by regulating the cathode excess oxygen ratio λ_{O_2}, which is a lumped variable.

We thus regulate the oxygen excess ratio λ_{O_2} in the FCS cathode by controlling the compressor motor voltage v_{cm} during step changes in current I_{st} drawn from the FCS. The control problem is challenging for two reasons. First, the topology of actuated, disturbance, and performance variables limits the disturbance rejection capabilities of any realizable controller. In particular, the variables manipulated by means of the actuator v_{cm} are upstream of where the disturbance I_{st} affects the performance variable λ_{O_2}. The second challenge arises from the fact that the traditionally used measurements for λ_{O_2} regulation are upstream of the performance variable due to difficulties in sensing within a vapor-saturated flow stream. To improve the system observability, we propose the use of FCS voltage in coordination with other feedback measurements. The proposed use of voltage by the feedback controller does not add cost to the overall system since voltage is already used in diagnostic and emergency shut-down procedures. Note that the FCS voltage cannot be used as the sole output-injection variable in the FCS observer because voltage depends on other variables such as hydrogen partial pressure [8], [19] and membrane humidification (dryness and flooding).

Apart from the air flow control design, we show that the closed-loop FC stack impedance resembles a passive resistive power source ($R_{st} = 0.05\,\Omega$) for current excitations slower than 0.1 rad/s. The FC impedance defines the power quality of the FCS as a power source [20] especially when the FCS is connected to sensitive electronic equipment or to a grid of heterogeneous power sources [20], [21]. Finally, we show that minimizing parasitic losses and providing fast air flow regulation are conflicting objectives. The conflict arises from the fact that the flow device uses part of the stack power to accelerate. One way to resolve this conflict is to augment the FCS system with an auxiliary battery or an ultracapacitor to drive the auxiliary devices or buffer the FCS from transient current demands. These additional components, however, introduce complexity and additional weight [4]. We analyze the tradeoff between the two objectives using a single-input, two-output (SITO) control configuration [22]. We then show that a compromise needs to be made between oxygen starvation and FCS net power for transients faster than 0.7 rad/s (see Figure 19). Although this number is specific to our system, our analysis procedure is general and can be applied to other FC systems.

Nonlinear Fuel Cell Stack System Model

In this section we present a nonlinear dynamic model of the FC system using electrochemical, thermodynamic, and zero-dimensional fluid flow principles documented in detail in [12] and [13]. We concentrate on the dynamical PEM-FC behavior associated with the reactant pressure and flow, and we neglect the slower dynamics associated with temperature regulation and heat dissipation. We assume that the averaged stack temperature T_{st} is well regulated for all phases modeling, analysis, and control design. We also assume that the inlet reactant flows in the cathode and anode can be humidified in a consistent and rapid way. Although the last assumption is not satisfied in practice, especially during fast transients, lack of experimental data prevents the accurate representation and analysis of dynamic coupling between temperature and humidity variations.

In this study, we assumed as shown in Figure 3 that the multiple cathode and anode volumes of FCs in the stack are lumped together as a single stack cathode and anode volume. Pressurized hydrogen is supplied to the FC stack anode through a pressure regulator. The anode supply and return manifold volumes are small, and the pure hydrogen flow allows us to lump these volumes into

one "anode" volume. We denote the variables associated with the lumped anode volume by the subscript "an." The cathode supply manifold (sm) lumps the volumes associated with pipes and connections between the compressor and stack cathode (ca). The cathode supply manifold volume in the Ford P2000 experimental vehicle is significant due to the long distance between the flow control device, located at the front of the vehicle, and the stack, located in the rear of the vehicle [10]. The cathode return manifold represents the lumped volume of pipes downstream of the stack cathode.

Nomenclature

The variables we use are listed below. Masses (kg) are denoted with m, mass flows (kg/s) with W, molar masses (kg/mol) with M, pressure (kPa) with p, temperatures (K) with T, vapor saturation pressure at temperature T_x with $p_{\text{sat}}(T_x) = p^x_{\text{sat}}$, relative humidity with ϕ, humidity ratio with Ω, rotational speed (rad/s) with ω, power (watts) with P, current (A) with I, current density (A/cm^2) with i, area (cm^2) with A, volume (m^3) with V, voltage (volts) with v. The variables associated with vapor are denoted with a subscript v, water with w, oxygen with O_2, nitrogen with N_2, and hydrogen with H_2. The variables in specific volumes have as a second subscript the volume identifier (sm,, ca, rm, an). The variables associated with the electrochemical reactions are denoted with "rct." The variables for the compressor or the compressor motor have "cp" or "cm," respectively, as their subscript. Similarly, the stack variables use "st," the individual FCs variables use "fc," the atmospheric variables use "atm," and the membrane variables use "mbr."

State-Space Representation

Mass conservation yields governing equations for oxygen, nitrogen, and water mass inside the cathode volume given by

$$\frac{dm_{O_2}}{dt} = W_{O_2,\text{in}} - W_{O_2,\text{out}} - W_{O_2,\text{rct}}, \tag{1}$$

$$\frac{dm_{N_2}}{dt} = W_{N_2,\text{in}} - W_{N_2,\text{out}}, \tag{2}$$

$$\frac{dm_{w,\text{ca}}}{dt} = W_{v,\text{ca,in}} - W_{v,\text{ca,out}} + W_{v,\text{gen}} + W_{v,\text{mbr}}. \tag{3}$$

The rate of change of the mass $m_{w,\text{ca}}$ of water inside the cathode depends solely on the summation of vapor flows, because it is assumed that the liquid water does not leave the stack and evaporates into the cathode gas if cathode humidity drops below 100%. The mass of water is in vapor form until the relative humidity of the gas exceeds saturation (100%), at which point vapor condenses into liquid water. The cathode pressure is then calculated using Dalton's law of partial pressures ($p_{\text{ca}} = p_{O_2} + p_{N_2} + p_{v,\text{ca}}$). The partial

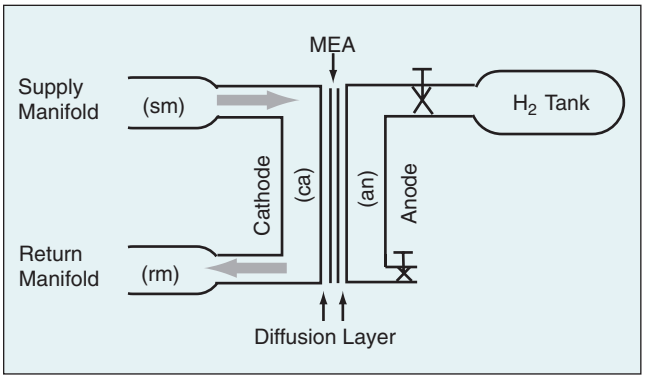

Figure 3. *Schematic of the fuel cell reactant supply system. The lumped parameter model uses four control volumes with spatially invariant time-varying variables.*

pressures for the oxygen ($p_{O_2} = (RT_{\text{st}})/(M_{O_2}V_{\text{ca}})m_{O_2}$), nitrogen ($p_{N_2} = (RT_{\text{st}})/(M_{N_2}V_{\text{ca}})m_{N_2}$), and vapor ($p_{v,\text{ca}} = \phi_{\text{ca}}p^{\text{st}}_{\text{sat}}$) in the cathode are algebraic functions of the states through the ideal gas law and the psychrometric laws since the cathode temperature is assumed to be fixed and equal to the overall stack temperature at $T_{\text{st}} = 353$ K (80 °C). Given the vapor saturation pressure $p^{\text{st}}_{\text{sat}}$, the relative humidity is $\phi_{\text{ca}} = \min[1, (m_{w,\text{ca}}RT_{\text{st}})/(p^{\text{st}}_{\text{sat}}M_vV_{\text{ca}})]$.

The flow rates into and out of the cathode are defined based on the difference between the pressures of the upstream and downstream gases. These relations are defined in the next section based on the states in the supply and the return manifold. In particular, the rate of change of mass m_{sm} inside the supply manifold is governed by mass conservation, and the rate of change p_{sm} of supply manifold pressure is governed by energy conservation modeled by

$$\frac{dm_{\text{sm}}}{dt} = W_{\text{cp}} - W_{\text{sm}}, \tag{4}$$

$$\frac{dp_{\text{sm}}}{dt} = \frac{\gamma R}{M^{\text{atm}}_a V_{\text{sm}}}(W_{\text{cp}}T_{\text{cp}} - W_{\text{sm}}T_{\text{sm}}), \tag{5}$$

where R is the universal gas constant, γ is the ratio of the specific heat capacities of air, M^{atm}_a is the molar mass of atmospheric air at ϕ_{atm}, V_{sm} is the manifold volume, and $T_{\text{sm}} = (p_{\text{sm}}V_{\text{sm}}M^{\text{atm}}_a)/(Rm_{\text{sm}})$ is the supply manifold gas temperature.

The flow and temperature out of the compressor (W_{cp} and T_{cp}) depend on the compressor rotational speed ω_{cp}, which is governed by the combined compressor motor inertia J_{cp} according to

$$J_{\text{cp}}\frac{d\omega_{\text{cp}}}{dt} = \frac{1}{\omega_{\text{cp}}}(P_{\text{cm}} - P_{\text{cp}}), \tag{6}$$

where P_{cm} and P_{cp} denote the power supplied to the compressor motor and the power required to drive the

compressor, respectively. The compressor motor power $P_{\rm cm}(v_{\rm cm}, \omega_{\rm cp})$ is calculated from the motor input voltage v_{cm}, which is the actuator signal. Other nonlinear maps are used to calculate the consumed compressor power $P_{\rm cp}(\omega_{\rm cp}, (p_{\rm sm})/(p_{\rm atm}), T_{\rm atm})$, the flow rate $W_{\rm cp}(\omega_{\rm cp}, (p_{\rm sm})/(p_{\rm atm}), T_{\rm atm})$, and flow temperature $T_{\rm cp}(\omega_{\rm cp}, (p_{\rm sm})/(p_{\rm atm}), T_{\rm atm})$. Numerical values for these nonlinear maps can be found in [23].

The state equation of the return manifold pressure is

$$\frac{dp_{\rm rm}}{dt} = \frac{RT_{\rm st}}{M_a^{\rm ca} V_{\rm rm}}(W_{\rm ca} - W_{\rm rm}), \tag{7}$$

where $V_{\rm rm}$ and $T_{\rm st}$ denote return manifold volume and gas temperature, respectively. Note that the isothermal assumption in the return manifold allows us to eliminate the state $m_{\rm rm}$, which now depends on p_{rm} according to the ideal gas law ($m_{\rm rm} = (p_{\rm rm} V_{\rm rm} M_a^{\rm ca})/(RT_{\rm st})$).

The governing equations for hydrogen and water in the anode can be written as

$$\frac{dm_{H_2}}{dt} = W_{H_2,\rm in} - W_{H_2,\rm purge} - W_{H_2,\rm rct}, \tag{8}$$

$$\frac{dm_{w,\rm an}}{dt} = W_{v,\rm an,in} - W_{v,\rm purge} - W_{v,\rm mbr}, \tag{9}$$

with the anode pressure and relative humidity calculated as

$$p_{an} = \underbrace{\frac{RT_{st}}{M_{H_2} V_{\rm an}} m_{H_2}}_{p_{H_2}} + \underbrace{\min\left[1, \frac{RT_{\rm st} m_{w,\rm an}}{M_v V_{\rm an} p_{\rm sat}^{\rm st}}\right]}_{\phi_{\rm an}} p_{\rm sat}^{\rm st}.$$

In summary, the nonlinear model based on the state equations (1)–(9) inolves the nine states

$$x_{\rm NL} = \left[m_{O_2}, m_{H_2}, m_{N_2}, \omega_{\rm cp}, p_{\rm sm}, m_{\rm sm}, m_{w,\rm an}, m_{w,\rm ca}, p_{\rm rm}\right]^T.$$

Reactant Flow Rates

The air temperature in the supply manifold $T_{\rm sm}$ from (4)–(5) is typically higher than the desired stack temperature $T_{\rm st}$ due to the high compressor exit temperature $T_{\rm cp}$. We assume that a "perfect" heat exchanger has been implemented to maintain the temperature of the cathode inlet-flow to the desired $T_{\rm st}$. Similarly, we assume that an instantaneous humidifier regulates the relative humidity of the cathode inlet-flow at the desired relative humidity $\phi_{\rm ca,in}^{\rm des}$ by injecting vapor. We employ these assumptions, despite their severity, to achieve basic understanding of the oxygen starvation problem by isolating the flow/pressure dynamics from the temperature and humidity dynamics. Future work will extend the model to include realistic heat exchanger and vaporizer characteristics.

The outlet mass flow rates of the supply manifold $W_{\rm sm}(p_{\rm ca}, p_{\rm sm}, T_{\rm sm})$, the cathode $W_{\rm ca}(p_{\rm rm}, p_{\rm ca}, T_{\rm st})$, and the return manifold $W_{\rm rm}(p_{\rm atm}, p_{\rm rm}, T_{\rm st})$ are calculated using nozzle equations [12].

Based on the gas outflow from the supply manifold, specifically, its mass flow rate $W_{\rm sm}$, pressure $p_{\rm sm}$, desired humidity $\phi_{\rm ca,in}^{\rm des}$, and temperature $T_{\rm st}$, along with the atmospheric air conditions $(p_{\rm atm}, T_{\rm atm}, \phi_{\rm atm}, \chi_{O_2})$, we calculate the individual species of (1)–(3) by means of

$$W_{O_2,\rm in} = y_{O_2} \frac{1}{1+\Omega_{\rm atm}} W_{\rm sm}, \tag{10}$$

$$W_{N_2,\rm in} = y_{N_2} \frac{1}{1+\Omega_{\rm atm}} W_{\rm sm}, \tag{11}$$

$$W_{v,\rm ca,in} = \frac{\Omega_{\rm ca,in}}{1+\Omega_{\rm atm}} W_{\rm sm}. \tag{12}$$

We define the mass fraction of oxygen and nitrogen in the dry atmospheric air as $y_{O_2} = \chi_{O_2} M_{O_2}/M_a^{\rm atm}$ and $y_{N_2} = (1-\chi_{O_2}) M_{N_2}/M_a^{\rm atm}$, where $M_a^{\rm atm} = \chi_{O_2} M_{O_2} + (1-\chi_{O_2}) M_{N_2}$ and $\chi_{O_2} = 0.21$ is the oxygen mole fraction in dry air. The atmospheric (at compressor inlet) and cathode inlet humidity ratio are given by

$$\Omega_{\rm atm} = \frac{M_v}{M_a} \frac{\phi_{\rm atm} p_{\rm sat}^{\rm atm}/p_{\rm atm}}{1 - \phi_{\rm atm} p_{\rm sat}^{\rm atm}/p_{\rm atm}}, \tag{13}$$

$$\Omega_{ca,\rm in} = \frac{M_v}{M_a} \frac{\phi_{\rm ca,in}^{\rm des} p_{\rm sat}^{\rm st}}{p_{\rm sm}(1 - \phi_{\rm atm} p_{\rm sat}^{\rm atm}/p_{\rm atm})}. \tag{14}$$

Also, the mass flow rate of each species out of the cathode is calculated as

$$W_{O_2,\rm out} = \frac{m_{O_2}}{m_{\rm ca}} W_{\rm ca}, \tag{15}$$

$$W_{N_2,\rm in} = \frac{m_{N_2}}{m_{\rm ca}} W_{\rm ca}, \tag{16}$$

$$W_{v,\rm ca,out} = \frac{p_{v,\rm ca} V_{\rm ca} M_v}{RT_{\rm st} m_{\rm ca}} W_{\rm ca}, \tag{17}$$

where $m_{\rm ca} = m_{O_2} + m_{N_2} + (p_{v,\rm ca} V_{\rm ca} M_v)/(RT_{\rm st})$ is the total mass of the cathode gas.

The oxygen reaction rate $W_{O_2,\rm rct}$, hydrogen reaction rate $W_{H_2,\rm rct}$, and water generation rate $W_{v,\rm gen}$ are calculated from the stack current $I_{\rm st}$ by using the electrochemical equations

$$W_{O_2,\rm rct} = M_{O_2} \frac{n I_{\rm st}}{4F}, \tag{18}$$

$$W_{H_2,\rm rct} = M_{H_2} \frac{n I_{\rm st}}{2F}, \tag{19}$$

$$W_{v,\rm gen} = M_v \frac{n I_{\rm st}}{2F}, \tag{20}$$

where n is the number of cells in the stack and F is the Faraday number ($F = 96,485$ C).

The mass flow $W_{v,\mathrm{mbr}}$ of vapor across the membrane is calculated using mass transport principles and membrane properties given in [24] according to

$$W_{v,\mathrm{mbr}} = M_v A_{\mathrm{fc}} n \left(n_d \frac{i}{F} - D_w \frac{(\phi_{\mathrm{ca}} - \phi_{\mathrm{an}})}{t_m} \right), \tag{21}$$

where A_{fc} is the active area of the FC and i is the FC current density (current per active area, $I_{\mathrm{st}}/A_{\mathrm{fc}}$). The variable $n_d(\phi_{\mathrm{ca}}, \phi_{\mathrm{an}})$ is the electro-osmotic coefficient, $D_w(\phi_{\mathrm{ca}}, \phi_{\mathrm{an}}, T_{\mathrm{st}})$ is the diffusion coefficient, and t_m is membrane thickness used in the work of [24] and [25] and documented in [12].

The anode inlet flow rate $W_{\mathrm{an,in}} = k_{p,\mathrm{an}}(p_{\mathrm{ca}} - p_{\mathrm{an}} + \delta p)$ is regulated to maintain a constant pressure difference δp across the membrane. This rate can be achieved by using high-gain proportional control with reference signal provided by the supply manifold pressure sensor. The hydrogen and water flows to the anode in (8)–(9) are calculated by

$$W_{H_2,\mathrm{in}} = \frac{1}{1 + \Omega_{\mathrm{an,in}}} W_{\mathrm{an,in}}, \tag{22}$$

$$W_{v,\mathrm{an,in}} = \frac{\Omega_{\mathrm{an,in}}}{1 + \Omega_{\mathrm{an,in}}} W_{\mathrm{an,in}}. \tag{23}$$

The anode inlet humidity ratio $\Omega_{\mathrm{an,in}}$ is calculated from the flow temperature $T_{\mathrm{an,in}}$, relative humidity $\phi_{\mathrm{an,in}}$, and pressure $p_{\mathrm{an,in}}$ of the flow leaving the hydrogen humidifier by means of

$$\Omega_{\mathrm{an,in}} = \frac{M_v}{M_{H_2}} \frac{\phi_{\mathrm{an,in}} p_{\mathrm{sat}}^{an,\mathrm{in}}}{p_{\mathrm{an,in}}}. \tag{24}$$

The relative humidity $\phi_{\mathrm{an,in}}$ is set to 50% to provide subsaturated conditions in the anode ($\phi_{\mathrm{an}} < 1$), which, in turn, prevents anode flooding. Under these conditions, the anode purge is disabled ($W_{v,\mathrm{purge}} = 0$).

Performance Variables

The nonlinear state equations in (10) have the form

$$\begin{aligned} \dot{x}_{\mathrm{NL}} &= f(x_{\mathrm{NL}}, u, w), && \text{(state equations)} \\ u &= v_{\mathrm{cm}}, && \text{(actuator (control) signals)} \\ w &= I_{\mathrm{st}}, && \text{(exogenous inputs)} \end{aligned}$$

where the control input u is the compressor motor voltage v_{cm}, and the disturbance input w is the current I_{st} drawn from the FCS. The performance variables are the net power $P_{\mathrm{net}} = P_{\mathrm{net}}^{\mathrm{ref}}(I_{\mathrm{st}})$ produced by the FCS system and the excess oxygen ratio $\lambda_{O_2} = \lambda_{O_2}^d$ in the FCS cathode. Both performance variables are defined below.

The FC voltage v_{fc} is given in the form of either polarization curves or a nonlinear map [12] of current density i and other anode and cathode variables as $v_{\mathrm{fc}}(i, p_{O_2}, p_{H_2}, T_{\mathrm{st}}, \phi_{\mathrm{ca}}, \phi_{\mathrm{an}})$. Figure 4 shows polarization curves for different values of oxygen partial pressure p_{O_2}. Since n FCs are connected in series to form an FC stack (FCS), the total FCS voltage and power are $v_{\mathrm{st}} = n v_{\mathrm{fc}}$ and $P_{\mathrm{st}} = n A_{\mathrm{fc}} v_{\mathrm{fc}} i$. The air compressor is the main contributor of parasitic loss in the FC system [17], therefore the net power obtained from the FC stack system is

$$P_{\mathrm{net}} = P_{\mathrm{st}}(x_{\mathrm{NL}}, I_{\mathrm{st}}) - P_{\mathrm{cm}}(x_{\mathrm{NL}}, v_{\mathrm{cm}}). \tag{25}$$

The oxygen excess ratio λ_{O_2} is then used as the lumped variable that indicates FCS oxygen starvation

$$\lambda_{O_2} = \frac{W_{O_2,\mathrm{in}}(x_{\mathrm{NL}})}{W_{O_2,\mathrm{rct}}(x_{\mathrm{NL}}, I_{st})}. \tag{26}$$

We explicitly denote the dependence on the input I_{st}, which directly affects $W_{O_2,\mathrm{rct}}$ and causes an instantaneous drop of λ_{O_2}. On the other hand, the actuator v_{cm} affects the oxygen excess ratio λ_{O_2} indirectly through the states x_{NL}. High λ_{O_2}, and thus high oxygen partial pressure, improves the total power P_{st} but also requires higher P_{cm}. Above an optimum λ_{O_2} level, that depends on I_{sts} [12], further increase of λ_{O_2} will cause a decrease in P_{net}. For simplification we assume the fixed value $\lambda_{O_2}^d = 2$. In the future, extremum-seeking or other maximum-finding techniques can be used to search on-line for the optimum excess oxygen ratio level.

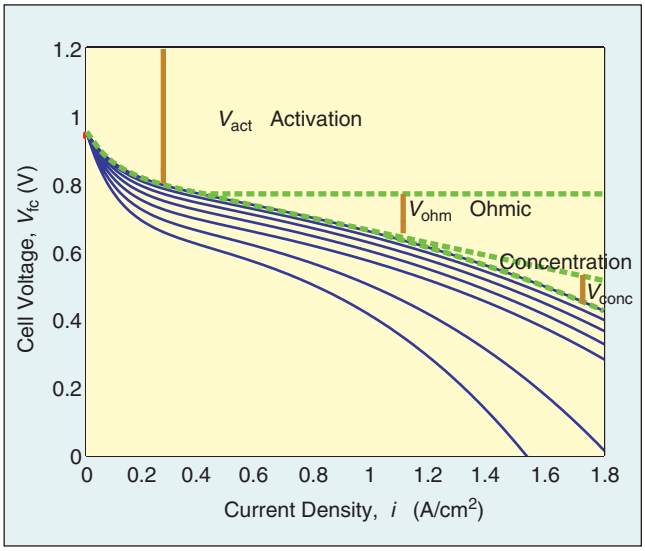

Figure 4. *FC polarization curves for different oxygen partial pressures. The cell voltage drops as the current density drawn from the fuel cell increases. The steady-state voltages depend on the activation, ohmic, and concentration losses. The losses increase when the partial pressure of oxygen in the cathode decreases.*

The overall control design objective is to define the compressor motor input voltage $v_{\rm cm}$ to maintain $\lambda_{O_2} = 2$ and achieve the desired FC system net power $P_{\rm net} = P_{\rm net}^{\rm ref}(I_{\rm st})$ based on a static map of the current drawn from the FCS. The potential measurements include air flow rate $W_{\rm cp}$ through the compressor, supply manifold pressure $p_{\rm sm}$, and stack voltage $v_{\rm st}$. The resulting control problem is given by

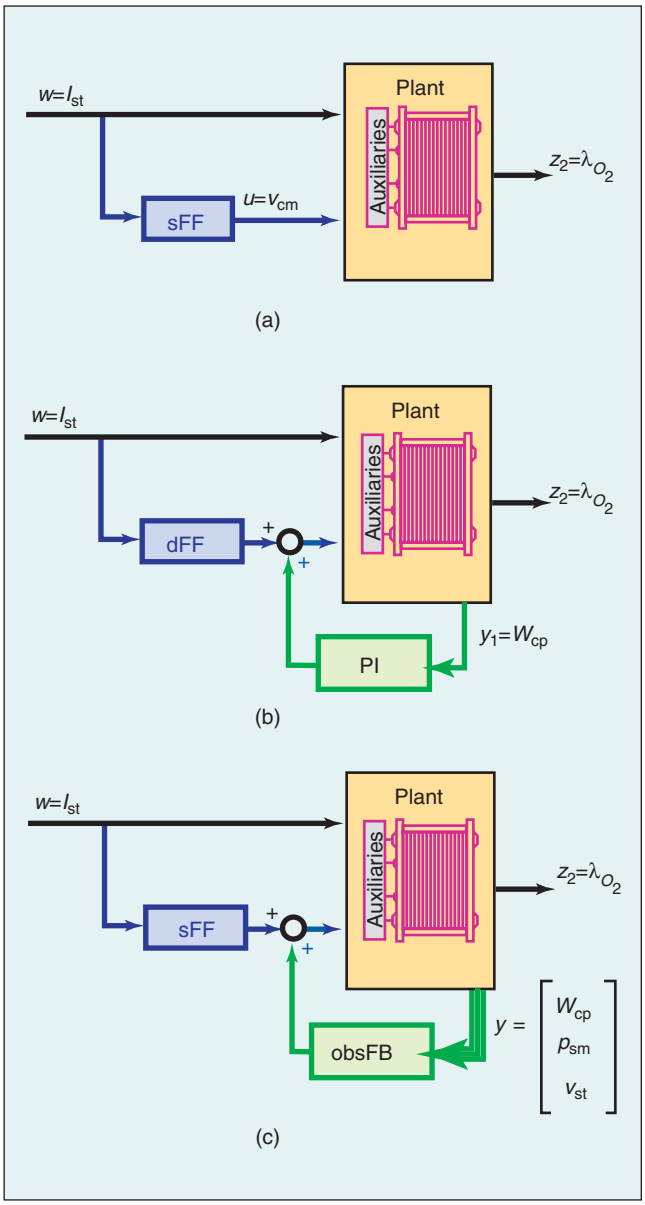

Figure 5. *Three different control configurations. Configuration (a) represents a steady-state feedforward control that can be implemented with a look-up table. Configuration (b) includes a dynamic feedforward controller, which achieves good transient regulation but lacks robustness to plant variations, and a PI feedback controller for steady state regulation. Configuration (c) includes observer-based feedback and a static feedforward controller.*

$$y = [W_{\rm cp}\, p_{\rm sm}\, v_{\rm st}]^T = h_y(x_{\rm NL}, u, w), \quad \text{(measurements)}$$
$$z = [e_{P_{\rm net}} \lambda_{O_2}]^T = h_z(x_{\rm NL}, u, w), \quad \text{(performance variables)}$$

where $e_{P_{\rm net}} = P_{\rm net}^{\rm ref} - P_{\rm net}$. Figure 2 illustrates the physical location of all of the input/output variables. First we focus on the problem of using the compressor motor voltage v_{cm} to regulate the oxygen excess ratio $\lambda_{O_2}^d = 2$. Next we consider two control objectives, namely, $e_{P_{\rm net}}^d = 0$ and $\lambda_{O_2}^d = 2$. Note that the two objectives are achievable at steady state, but not during transients, by a single control actuator. The tradeoff between the performance variables $e_{P_{\rm net}}$ and λ_{O_2} is presented at the end of this article.

Control Configurations

We consider three different control schemes for the FC stack system as illustrated in Figure 5. Because the disturbance (stack current) can be measured, a static function that correlates the steady-state value between the control input v_{cm} and the disturbance $I_{\rm st}$ can be used in the feedforward path. This static feedforward (sFF) scheme shown in Figure 5(a) is easily implemented with a look-up table. The static feedforward controller determines the compressor voltage command $v_{\rm cm}^*$, which achieves an air flow that replenishes the oxygen flow depleted during a current command $I_{\rm st}$. For specific ambient conditions of pressure, temperature, and humidity, the required air flow can be calculated analytically from the stack current $W_{\rm cp}^* = f_{\rm cp}(I_{\rm st})$ based on electrochemical and thermodynamic principles modeled by

$$\begin{aligned} W_{\rm cp}^* &= (1 + \Omega_{\rm atm}) W_{\rm air}^* \\ &= \left(1 + \frac{M_v}{M_a^{\rm atm}} \frac{\phi_{\rm atm} p_{\rm sat}^{\rm atm}}{(p_{\rm atm} - \phi_{\rm atm} p_{\rm sat}^{\rm atm})}\right) \frac{1}{\chi_{O_2}} \lambda_{O_2} M_{O_2} \frac{n I_{\rm st}}{4F}. \end{aligned} \tag{27}$$

Analytical modeling or experimental testing can be used to construct the inverse of compressor and compressor motor maps to find $v_{\rm cm}^* = f_{\rm cm}(I_{\rm st})$ that the desired air flow $W_{\rm cp}^*$. In this article we use nonlinear simulation to determine the static feedforward controller sFF that cancels the effect of the current disturbance $w = I_{\rm st}$ to the oxygen excess ratio $z_2 = \lambda_{O_2}$ at steady state.

When an analytical model of the FCS is available, a dynamic feedforward controller can be designed to achieve better transient response. In particular, a linear dynamic feedforward controller (dFF) that cancels the effect of w to z_2 over a wide range of frequencies is designed first. A proportional integral feedback controller (PI) is designed to reduce sensitivity to modeling error, device aging, and variations in ambient conditions. As discussed later, the PI feedback controller must be sufficiently slow so that the transient response of the combined dFF+PI controller does not deteriorate. The need for a small integral gain arises from the fact

that the PI controller acts on the compressor flow $y_1 = W_{\rm cp}$ upstream of the cathode inlet air flow $W_{\rm sm}$, which directly affects the performance variable $z_2 = \lambda_{O_2}$ through (10) and (26). Unfortunately, $W_{\rm sm}$ is difficult to measure due to the high relative humidity in the cathode inlet conditions.

In the following sections we also study the performance of observer-based and integral-augmented feedback control architecture. A feedback controller is combined with the static feedforward controller as shown in Figure 5(c) to form the sFF+obsFB controller whose order is similar to the order of the dFF+PI controller. We show that an observer-based feedback that uses only the air flow measurement $y_1 = W_{\rm cp}$ achieves marginally higher closed-loop bandwidth than the simple PI feedback controller. Significant improvement of the closed-loop bandwidth is achieved by measuring the stack voltage and using this signal in the observer-based feedback controller. The multiple measurements allow better observability of the system states and, consequently, better regulation of the transient excess oxygen ratio $z_2 = \lambda_{O_2}$.

Linearization

We linearize the nonlinear system (1)–(26) at the nominal operating point with net power $z_1^o = 40$ kW and oxygen excess ratio $z_2^o = 2$. The inputs that correspond to this operating point are a stack current of $w^o = 191$ A, and a compressor motor voltage of $u^o = 164$ V. The linear model is given by

$$\begin{aligned} \delta\dot{x} &= A\delta x + B_u\delta u + B_w\delta w, \\ \delta z &= C_z\delta x + D_{zu}\delta u + D_{zw}\delta w, \\ \delta y &= C_y\delta x + D_{yu}\delta u + D_{yw}\delta w, \end{aligned} \tag{28}$$

where $\delta(\cdot) = (\cdot) - (\cdot)^o$ represents deviation from a nominal value. The state x, measurements y, performance variables z, input u, and disturbance w, are defined by

$$\begin{aligned} x^T &= \left[m_{O_2}, m_{H_2}, m_{N_2}, \omega_{cp}, p_{\rm sm}, m_{\rm sm}, m_{w,\rm an}, p_{rm}\right], \\ y^T &= [W_{\rm cp}, p_{\rm sm}, v_{\rm st}], \quad z^T = [e_{P\rm net}, \lambda O_2], \\ u &= v_{\rm cm}, \quad w = I_{\rm st}. \end{aligned}$$

The units of states and outputs are scaled so that all states have comparable magnitudes: mass in grams, pressure in bar, rotational speed in kRPM, mass flow rate in gallons per second, power in kilowatts, voltage in volts, and current in amps. Note that the resulting linear model has eight states, whereas the nonlinear model has nine states. The mass $m_{w,\rm ca}$ of water in the cathode is removed because it is unobservable after linearization. The reason is as follows: With the membrane parameters in (21), there is excessive water flow from anode to cathode that results in fully humidified cathode gas. Thus, for constant temperature, the vapor pressure is constant and equal to the saturated vapor pressure. Moreover, the nonlinear model does not include the effects of liquid condensation, also known as "flooding," on any of the measurements or performance variables.

There are two linearization cases. The first is the regular input/output linearization of the plant with $(A, B_u, B_w, \ldots, D_{zw})$ as in (28). This model is used in the next section to design the dynamic feedforward controller in Figure 5(b). The second linearization is performed to include the static feedforward map $f_{\rm cp}(w)$. The corresponding matrices $(A, B_u, B_w^o, \ldots, D_{zw}^o)$ are used in the following sections to design the observer-based feedback controller shown in Figure 5(c). As our notation indicates, the matrices of the two systems are the same, with the following exceptions: $B_w^o = ((\partial f/\partial w) + (\partial f/\partial u)(\partial f_{cp}/\partial w))|_{x^o,u^o,w^o} = B_w + B_u(\partial f_{cp}/\partial w)|_{w^o}$ and $D_{z_1w}^o = D_{z_1w} + D_{z_1u}(\partial f_{cp}/\partial w)|_{w^o}$. Note that D_{z_2w} is the same for both cases since $D_{z_2u} = 0$. For both linear systems, the proportional anode flow control is included in the linearization.

Dynamic Feedforward

Due to the topology of the control input $u = v_{cm}$ and the disturbance $w = I_{\rm st}$ with respect to the performance variable $z_2 = \lambda_{O_2}$, the disturbance rejection capabilities of the open-loop system are moderate. In particular, the control signal $u = v_{cm}$ affects the performance variable $z_2 = \lambda_{O_2}$ through the dynamics associated with the compressor inertia, supply manifold filling, and, eventually, cathode manifold filling as shown in Figure 2. On the other hand, the disturbance $w = I_{\rm st}$ affects the performance variable $z_2 = \lambda_{O_2}$ directly (see Figure 2 and (26)). To achieve good disturbance rejection, the control variable u needs to use a lead filter for the measured disturbance w based on the inversion of the open-loop dynamics [26].

The linear system can be arranged in the transfer function form

$$\Delta Z_2 = G_{z2u}\Delta U + G_{z2w}\Delta W, \tag{29}$$

where $G_{z2u}(s) = C_{z_2}(sI - A)^{-1}B_u$ and $G_{z2w}(s) = C_{z_2} \times (sI - A)^{-1}B_w + D_{z_2w}$, and all upper-case variables are in the Laplace domain. Let a dynamic feedforward controller be $\Delta U = K_{uw}\Delta W$, as shown in Figure 6.

The transfer function from W to Z_2 can be written as

$$T_{z_2w} = \frac{\Delta Z_2}{\Delta W} = (G_{z2w} + G_{z2u}K_{uw}). \tag{30}$$

For perfect disturbance rejection, that is, $T_{z_2w} = 0$, the feedforward controller $K_{uw}^{\rm ideal}$ is given by

$$K_{uw}^{\rm ideal} = -G_{z2u}^{-1}G_{z2w}. \tag{31}$$

Since the open-loop plant dynamics G_{z2u} is minimum phase and G_{z2w} is stable, $K_{uw}^{\rm ideal}$ is a stable controller.

Either modification of the current disturbance or techniques from [27] and [28] can be used in the case of a delay or nonminimum phase system dynamics. The inverse of the G_{z2u} transfer function calculated in (31) is not proper and thus not realizable. Moreover, K_{uw}^{ideal} uses high gain at high frequencies. To obtain a strictly proper controller K_{uw}, high-frequency components of K_{uw}^{ideal} are removed using a low-pass filter with break frequencies at 80, 120, and 120 rad/s. By increasing the filter break frequencies, the response of z_2 can be made faster at the expense of large control action.

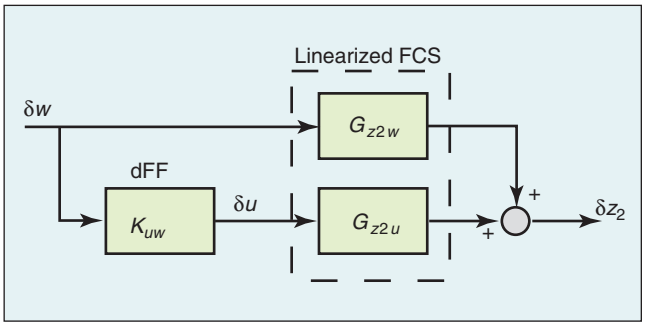

Figure 6. *Dynamic feedforward control. The feedforward controller changes the compressor voltage to replenish the oxygen depleted from the cathode by the current. Regulation is achieved by approximate inversion of the air path dynamics.*

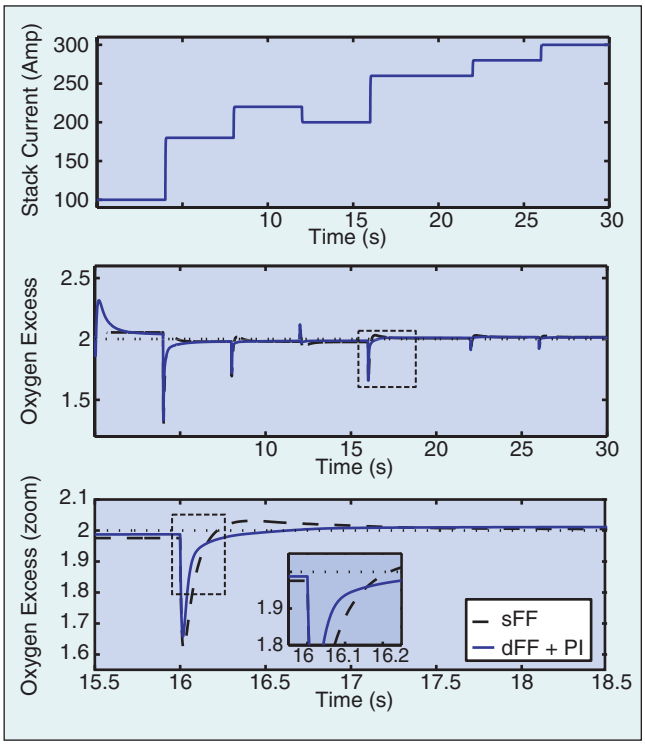

Figure 7. *Response of FCS with dynamic feedforward and PI controller in nonlinear simulation during step changes in current. The response with a static feedforward sFF controller (dashed line) is shown for comparison.*

Even though the dynamic feedforward controller cancels the effect of w to z_2 at a wide range of frequencies, the model-based inversion can adversely affect the disturbance rejection capability in the presence of unknown disturbances, modeling errors, and parameter variations. Because there is no feedback, the sensitivity function of the system with respect to unknown disturbances is equal to unity at all frequencies. The frequency domain modifications in [29] can be used to reduce the cancellation controller sensitivity if bounds on the size of the plant uncertainties are available. In this article, we use a PI controller to reduce the closed-loop sensitivity at low frequencies and ensure that the W_{cp} flow reaches the desired value $W_{\text{cp}}^* = f_{\text{cp}}(I_{\text{st}})$ at steady state. The dFF+PI controller is given by

$$U = K_{uw}\left(I_{\text{st}} - I_{\text{st}}^o\right) + \left(k_{p,\text{ca}} + \frac{k_{I,\text{ca}}}{s}\right)\left(W_{\text{cp}}^* - W_{\text{cp}}\right). \quad (32)$$

Since increasing the weighting gain $k_{I,\text{ca}}$ on the integrator degrades the speed of response $z_2 = \lambda_{O_2}$, a small integral $k_{I,\text{ca}}$ is used. The reason for the response degradation of the performance variable $z_2 = \lambda_{O_2}$ is that the integrator is applied to the air flow measurement $y_1 = W_{\text{cp}}$ far upstream from the point at which $z_2 = \lambda_{O_2}$ is defined (see Figure 2). Moving the flow measurement closer to the FC stack (either flow entering or exiting) is more appropriate in terms of control design, but is problematic due to high vapor concentration and potential condensation on the sensor [30].

Figure 7 shows the response of the nonlinear system with the dFF+PI controller subjected to a series of current steps. The dFF+PI controller has better disturbance rejection capability (from $w = I_{st}$ to $z_2 = \lambda_{O_2}$) than the static feedforward (sFF). After an initial excursion, which cannot be avoided as long as a causal controller is implemented, the dFF+PI returns λ_{O_2} to the 0.2% band of the desired λ_{O_2} within 0.04 s, whereas the sFF returns λ_{O_2} within 0.075 s. These response data show that the dFF+PI system is approximately twice as fast as the system with the static feedforward controller (sFF). Calibration and implementation of the PI controller is straightforward. However, the simplicity of this control configuration usually results in reduced system robustness (see Figure 11) since the control performance relies more on the feedforward path. In an effort to design a better (higher bandwidth) feedback controller, we next explore an observer-based feedback control design.

Observer-Based Feedback Control Design

The feedback controller is based on linear-quadratic techniques, which decompose the design problem into state feedback and observer synthesis using the separation principle. The linear model obtained from linearization with the static feedforward (sFF) is used to design the feedback

controller. Note here that we use the sFF and not the dFF in the linear model to minimize the order of the observer-based feedback controller.

State Feedback

The linear quadratic regulator (LQR) algorithm is used to design the state feedback controller. Integral control is combined with state feedback to reduce the steady-state error of the control output. Since the performance variable λ_{O_2} cannot be measured, integral control must be applied to one of the available measurements. The most obvious choice is to integrate the compressor flow rate $y_1 = W_{\rm cp}$ for two reasons: First, it is easy to measure $W_{\rm cp}$. Second, it is relatively easy to calculate the compressor air flow rate $W^*_{\rm cp} = f_{\rm cp}(I_{\rm st})$ that satisfies the desired oxygen excess ratio from (27). This calculation is based on electrochemical and thermodynamic calculations for known ambient conditions. The resulting state equation for the integrator is thus

$$\dot{q} = W^*_{\rm cp} - W_{\rm cp}. \tag{33}$$

The cost function

$$J = \int_0^\infty \delta\hat{x}^T C_{z_2}^T Q_{z_2} C_{z_2} \delta\hat{x} + q^T Q_I q + \delta u^T R \delta u \, dt \tag{34}$$

is used for the state feedback

$$\delta u = -K\left[\delta\hat{x}, q\right]^T = -K_p \delta\hat{x} - K_I q, \tag{35}$$

where the controller gain is $K := R^{-1}\hat{B}_u^T\bar{P}$ and $\bar{P}$ satisfies the algebraic Riccati equation (ARE)

$$\bar{P}\hat{A} + \hat{A}^T\bar{P} + \hat{Q}_x - \bar{P}\hat{B}_u R^{-1}\hat{B}_u^T\bar{P} = 0, \tag{36}$$

where $\hat{A} = [A, 0\,;\, -C_{y_1}, 0]$, $\hat{B}_u = [B_u; 0]$, $\hat{Q}_x = \text{diag}\,(Q_x, Q_I)$, and $Q_x = C_{z_2}^T Q_{z_2} C_{z_2}$.

The integral gain is set to a small value for the same reasons discussed in the dynamic feedforward design section. Due to the fact that there is disturbance feedthrough on the performance variable [see (28)], we add a pre-compensator u_p [31], [32], which modifies the control input u according to

$$\begin{aligned} u &= u^* + u_p - K[\delta\hat{x}, q]^T, \\ u_p &= \left[C_{z_2}(A - B_u K_p)^{-1} B_u\right]^{-1} \\ &\quad \times \left[D_{z_2 w} - C_{z_2}(A - B_u K_p)^{-1} B_w\right]. \end{aligned} \tag{37}$$

The linear closed loop response λ_{O_2} of the system with the full-state feedback controller sFF+stateFB in (37) is twice as fast as the open loop with the static feedforward controller sFF ($u = u^*$) as shown in Figure 8. The time response achieved by dFF+PI controller is not shown in Figure 8 because it is practically identical to the time response achieved with the full state feedback controller sFF+stateFB. The magnitude of the closed loop frequency response from the disturbance $w = I_{\rm st}$ to the performance variable $z_2 = \lambda_{O_2}$ is shown in Figure 9. It can be seen that the sFF+stateFB controller reduces the magnitude of $z_2 = \lambda_{O_2}$ at frequencies between 0.5 and 40 rad/s.

To prevent stack starvation, the stack current signal is typically filtered by a low-pass filter to allow enough time for the air supply system to increase air flow to the cathode. Since this solution slows down the FC power response, it is desirable to use the highest possible cutoff frequency in the low-pass filter such that fast current can be drawn without starving the stack. As can be seen from Figure 9, to reduce the magnitude of the excess ratio, the current filter used for the controlled system can have a higher cutoff frequency, which means that the controlled system can handle faster current draw. To completely

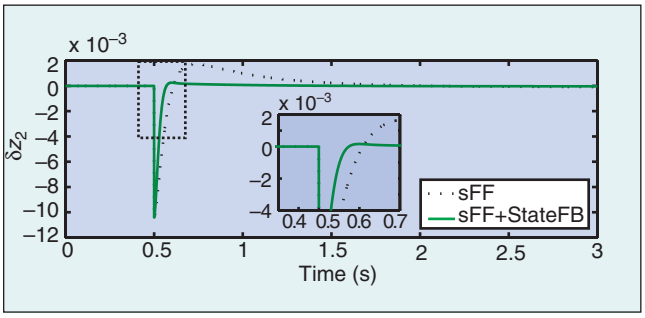

Figure 8. *Unit step response of system with full state feedback in linear simulation. The dashed line shows the system response with the nonlinear static feedforward sFF controller. The comparison demonstrates that the addition of state feedback achieves faster regulation with small overshoot in oxygen excess ratio.*

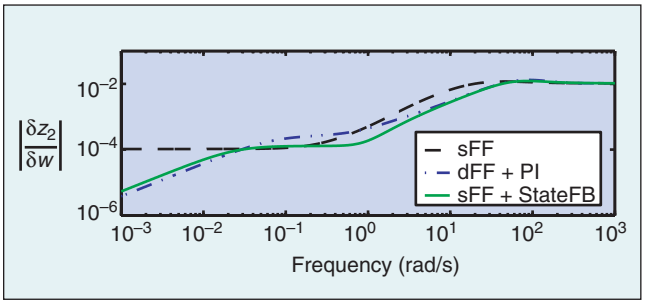

Figure 9. *Magnitude of closed-loop frequency response from w to z_2. The dashed and the dash-dot lines show the system response with the static feedforward (sFF) and the system response with the dynamic feedforward (dFF) plus PI controller, respectively. The comparison demonstrates that the static feedforward with state feedback (solid line) reduces the magnitude of $z_2 = \lambda_{O_2}$ at frequencies between 0.5 and 40 rad/s (0.08 to 6.4 Hz).*

avoid stack starvation, the closed-loop system can be combined with a current limiter using a reference governor [33] or a model predictive controller [34].

The fuel cell stack voltage signal contains high-frequency information about the oxygen utilization, and thus is a natural and valuable output for feedback.

Observer Design

The estimate $\delta\hat{x}$ of the state used in the calculation of the control input by (37) is determined using a state observer based on a stationary Kalman estimator design. The available measurements are compressor air flow rate $y_1 = W_{\rm cp}$, supply manifold pressure $y_2 = p_{\rm sm}$, and FC stack voltage $y_3 = v_{\rm st}$ (see Figure 2).

The requisite observability analysis is performed in [13], which shows the system eigenvalues λ_i, the corresponding eigenvectors, and the corresponding rank and condition number of

$$[\lambda_i I - A \quad C_y]^T \tag{38}$$

for three different cases: 1) measuring only y_1, 2) measuring y_1 and y_2, and 3) measuring y_1, y_2, and y_3. The dynamics associated with an eigenvalue are unobservable if the corresponding matrix (38) loses rank [35, sect. 2.4]. In this sense the corresponding eigenvalue is unobservable. A large condition number implies that a matrix is almost rank deficient. Thus, the large condition number of the matrix (38) indicates a weakly observable eigenvalue λ_i.

Comparing cases 1 and 2 shows that adding the measurement y_2 does not affect the observability. The eigenvectors associated with the two unobservable eigenvalues with measurements y_1 and y_2 suggest that the unobservable mode corresponds to the mass $m_{w,\rm an}$ of vapor in the anode. This observation agrees with the fact that the two measurements are in the air supply side, and the only connection to the water in the anode is a small membrane water flow. The hydrogen mass is more observable through the anode flow control, which regulates anode pressure following cathode pressure. Since these unobservable eigenvalues are fast, they have minimal effect on the observer performance. On the other hand, two slow eigenvalues –1.65 and –1.40 degrade observer performance because they are weakly observable, as indicated by their large condition numbers.

Adding the stack voltage measurement improves the state observability, as can be seen from the rank and the condition number for case 3. Although measuring the supply manifold pressure does not significantly improve the system observability, we nevertheless include this measurement because of its importance in regulating the anode pressure.

The high condition number for the slowest eigenvalue can degrade observer performance even in the case of three measurements. Many design iterations confirm the degradation. When this eigenvalue is moved, the resulting observer gain is large, and thus produces a large observer error overshoot. To prevent high observer gain, we design a reduced-order output estimator (closed-loop observer) for the observable part and an input estimator (open-loop observer) for the weakly observable part. Below, the design process for the case of three measurements is explained.

First, the system matrices are transformed to the modal canonical form $\delta\tilde{x} = T\delta x$ [36] such that the new system matrices are

$$\tilde{A} = TAT^{-1} = \begin{bmatrix} \lambda_1 & & 0 \\ & \ddots & \\ 0 & & \lambda_8 \end{bmatrix}, \tag{39}$$

$$\tilde{C} = C_y T^{-1}, \quad \tilde{B} = T[B_w \; B_u]. \tag{40}$$

Note the special structure of the matrix $\tilde{A}$, whose eigenvalues appear on the diagonal. The matrices are then partitioned into

$$\begin{bmatrix} \tilde{A}_o & 0 \\ 0 & \tilde{A}_{\bar{o}} \end{bmatrix}, \quad \begin{bmatrix} \tilde{B}_o \\ \tilde{B}_{\bar{o}} \end{bmatrix}, \quad \begin{bmatrix} \tilde{C}_o & \tilde{C}_{\bar{o}} \end{bmatrix}, \tag{41}$$

where $\tilde{A}_{\bar{o}} = \lambda_8 = -1.40$. The reduced-order observer gain $\tilde{L}$ is then designed for the matrices $\tilde{A}_o$, $\tilde{B}_o$, and $\tilde{C}_o$ by means of

$$\begin{aligned} \tilde{L} &:= \tilde{S}\tilde{C}_o^T\tilde{W}_y^{-1}, \\ 0 &= \tilde{S}\tilde{A}_o^T + \tilde{A}_o\tilde{S} + \tilde{V}_x + \tilde{S}\tilde{C}_o^T\tilde{W}_y^{-1}\tilde{C}_o\tilde{S}. \end{aligned} \tag{42}$$

The chosen weighting matrices are

$$\tilde{V}_x = \text{diag}[0.01 \; 10 \; 10 \; 0.01 \; 10 \; 10 \; 10] + \alpha \, \tilde{B}_o \, \tilde{B}_o^T, \tag{43}$$

$$\tilde{W}_y = 1 \times 10^{-6}\text{diag}[10 \; 100 \; 1], \tag{44}$$

which correspond to the process noise and the measurement noise, respectively, in the stochastic Kalman estimator design [37]. The matrix $\tilde{V}_x$ is in the form used in the feedback loop recovery procedure [38]. The reduced-order observer gain $\tilde{L}$ is then transformed to the original coordinate by means of

$$L = T^{-1}[\tilde{L} \quad 0]^T. \tag{45}$$

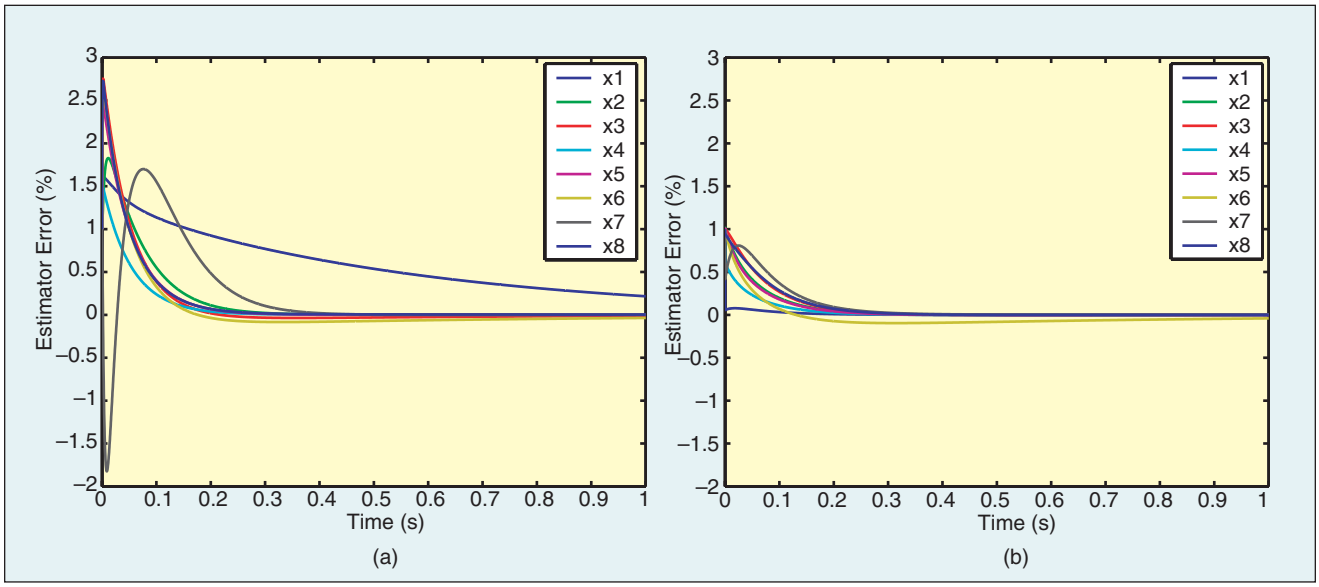

Figure 10. *Observer state error for different sets of measurements. (a) shows the observer error with compressor flow measurement. (b) shows the observer error with three measurements, namely, compressor flow, supply manifold pressure, and stack voltage.*

Figure 10(a) shows the response of the observer error based on three measurements in linear simulation. The initial errors of all states are set at 1% of maximum possible deviation from the nominal point. It can be seen that most of the states converge within 0.4 s. There is one slowly converging state caused by the weakly observable eigenvalue $\lambda_8 = -1.40$. Figure 10(b) shows the observer response when using one measurement $y_1 = W_{cp}$. Large overshoot and slow convergence can be observed.

Figure 11 shows that the sFF+obsFB1 controller with the single measurement $y_1 = W_{cp}$ does not reduce the input sensitivity function as well as the sFF+obsFB3 controller. Although, the loop transfer recovery method [38] can be used to bring the input sensitivity closer to that of full state feedback, the convergence rate of the observer is compromised. The sFF+obsFB1 controller has better bandwidth than the dFF+PI controller, but the full potential of the model-based controller is realized when the voltage measurement $y_3 = v_{st}$ is included in the feedback. In particular, Figure 11 shows that sFF+obsFB3 recovers the full-state-feedback sensitivity.

Simulations of the nonlinear system with different controllers are shown in Figure 12. Good transient response is achieved by both dynamic feedforward control (dFF+PI) and feedback control with three measurements (sFF+obsFB3). However, the feedback configuration is superior in term of robustness. The analysis of the performance and robustness of the feedback controller indicates that the voltage measurement should be used for feedback.

Different control configurations were considered in this first part of the paper, and the features and properties of each control design were presented. Because of its good performance and robustness, the observer-based feedback with the FCS voltage measurement is used in the remaining sections.

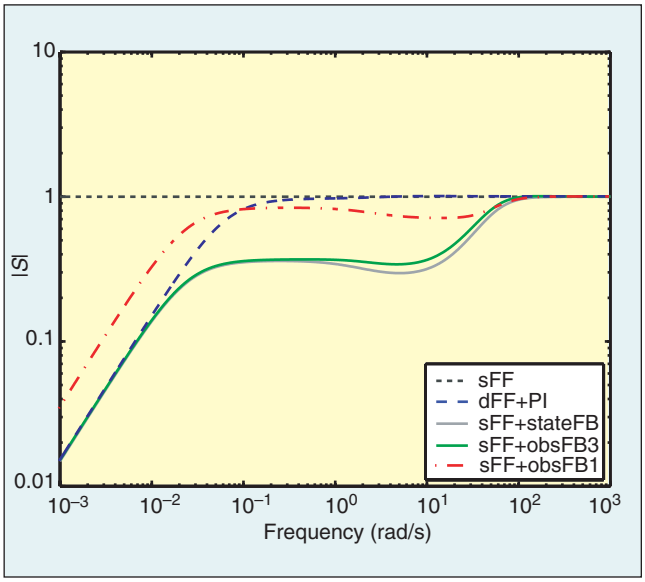

Figure 11. *Input sensitivity function for different controllers. The sensitivity of the dynamic feedforward plus PI (dFF+PI) and various dynamic output feedback controllers (sFF+obsFBx) is necessarily smaller than the sensitivity associated with the static feedforward controller (sFF with dotted line), and larger than the sensitivity associated with the full state feedback (sFF+stateFB with solid-thin line). The dynamic output feedback controller with the voltage measurement (sFF+obsFB3) recovers the sensitivity of the full state feedback controller as shown by the two solid lines.*

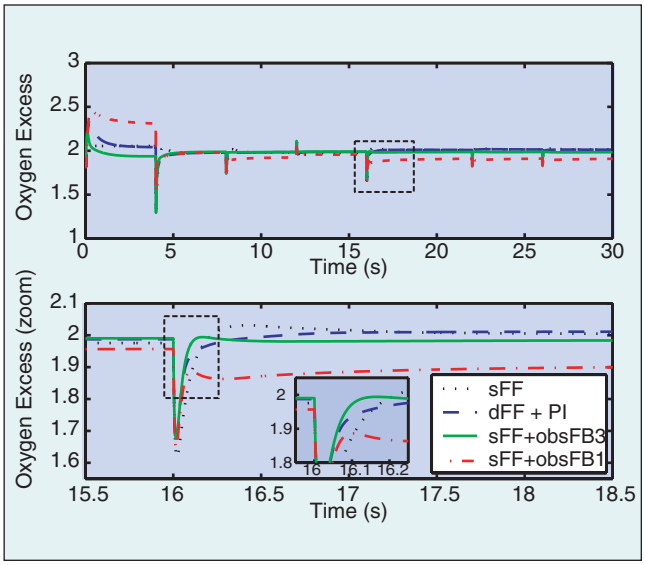

Figure 12. *Nonlinear simulation of FCS with different controllers. Using steady-state feedforward control plus the dynamic output feedback control with measured voltage (sFF+obsFB3, solid line) achieves fast regulation of the oxygen excess ratio.*

Closed-Loop Fuel Cell Impedance

In this section we calculate the impedance of the closed-loop FC system comprised of i) the air flow controller sFF+obsFB3 with the observer-based feedback described above, ii) the simple proportional anode pressure controller, and iii) the perfect cathode humidification incorporated in the model in (12) and (14). Figure 13 shows a schematic of the closed-loop FC system, which can now be viewed as a voltage source by the power management system.

The voltage of the controlled FCS (cFCS) can be written as $v_{\rm st}(t) = v_{\rm st}^o + \mathcal{L}^{-1}(Z_{\rm cFCS}(s)\Delta I_{\rm st}(s))$, where $Z_{\rm cFCS}(s)$ is the impedance of the cFCS and $\mathcal{L}$ denotes the Laplace operator. Figure 14 shows the Bode magnitude and phase of $Z_{\rm cFCS}(s)$. Electrochemical impedances are sometimes also shown with Nyquist plots (see for example [39], [40]) and used to identify the FCS performance for different material selection. The Bode plot in Figure 14 indicates that the cFCS can be represented by a passive resistance $|Z_{\rm cFCS}(\omega_{\rm low})| = R_{\rm cFCS}^{\rm low} = 0.05$ Ohm for current commands slower than 0.1 rad/s. A passive resistance of $|Z_{\rm cFCS}(\omega_{\rm high})| \approx R_{\rm cFCS}^{\rm high} = 0.3\ \Omega$ can also be used for current commands faster than 10 rad/s.

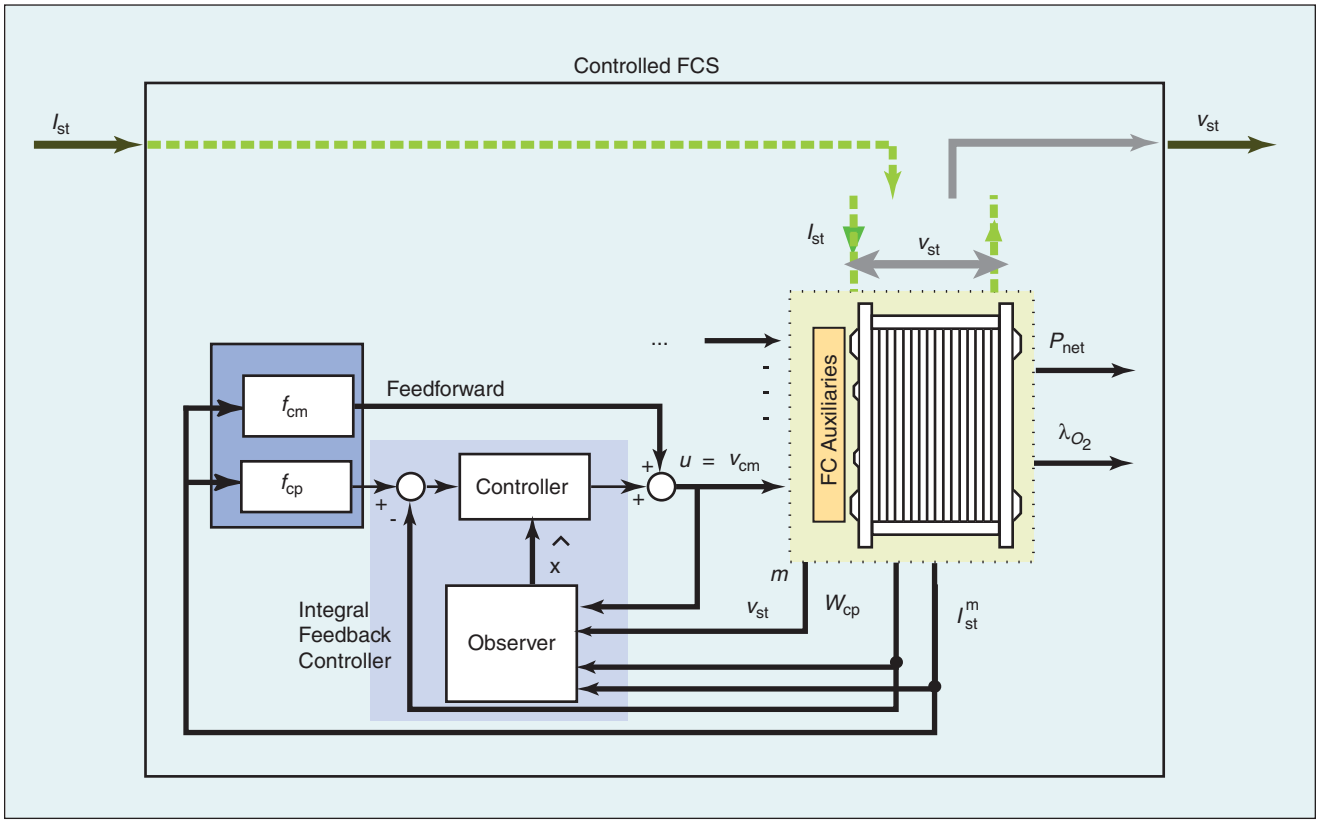

Figure 13. *Controlled FC stack as viewed by the power management system. The schematic drawing emphasizes the air flow controller. Other important subsystems that affect the FC stack impedance are the water and thermal management control loops and the anode supply.*

A plot of current-voltage trajectories against non-controlled FCS polarization curves is shown in Figure 15. Immediately after a step change in current, the voltage drops along the fixed cathode pressure polarization curve based on the high frequency impedance $R_{\text{cFCS}}^{\text{high}} = 0.3\ \Omega$. After the initial transient, the controlled FCS shows a voltage that transitions to another polarization curve of higher cathode pressure. This behavior is the reason for smaller cFCS resistance $R_{\text{cFCS}}^{\text{low}} = 0.05\ \Omega$ at low frequencies. The increase in operating cathode pressure is dictated by the λ_{O_2} regulation. This phenomenon is associated with the high pressure air supply through a high speed compressor. A low pressure FCS will have similar controlled and uncontrolled impedances, primarily due to the approximately constant operating pressure.

Tradeoff Between Two Performance Objectives

When there is no additional energy storage device, such as a battery or ultra-capacitor, the power used to run the compressor motor needs to be taken from the FC stack. A transient step change in stack current requires rapid increase in air flow to prevent depletion of cathode oxygen. The rapid air flow increase, consequently, requires a large amount of power drawn by the compressor motor (P_{cm}) and thus increases parasitic loss, which affects the system net power $P_{\text{net}} = P_{\text{FC}} - P_{\text{cm}}$.

The control problem we have considered so far is the single-input, single-output (SISO) problem of controlling the compressor voltage $u = v_{\text{cm}}$ to regulate the oxygen excess ratio $z_2 = \lambda_{O_2}$. Achieving the desired value of $z_2 = \lambda_{O_2}$ during steady-state ensures that the desired net power $z_1 = P_{\text{net}}$ is obtained. During transient, however, the two objectives are independent, resulting in the single-input two-output (SITO) control problem [22] shown in Figure 16.

Let us first consider the effects of the exogenous input I_{st} and the control signal v_{cm} on the first performance variable $z_1 = P_{\text{net}}(I_{\text{st}}, v_{\text{cm}}) = P_{\text{FC}}(I_{\text{st}}, v_{\text{cm}}) - P_{cm}(v_{\text{cm}})$, or, in the linear sense, $\delta z_1 = G_{z_1 w}\delta w + G_{z_1 u}\delta u$. As can be seen from the step responses in Figure 17, I_{st} has a positive effect on the net power. On the other hand, the compressor voltage v_{cm} causes an initial inverse response in the net power due to a nonminimum phase zero. The last plot in Figure 17 shows the net power during a step change in I_{st}, together with a step change in v_{cm}, which in steady-state ensures that $z_2 = \lambda_{O_2}^d = 2$. It can be seen that the time needed for P_{net} to reach the desired value is approximately one second.

It is apparent that to speed up the P_{net} response, we need either a larger magnitude of I_{st} to increase stack power or smaller value of v_{cm} to decrease the parasitic losses. Both cases degrade the speed of λ_{O_2} response, because larger I_{st} causes additional drops in λ_{O_2}, while smaller v_{cm} slows down the recovery rate of λ_{O_2}. The tradeoff between P_{net} and λ_{O_2} responses always exists because there is only one control actuator. The actuator must compromise between the two conflicting performance variables.

We systematically explore the tradeoff by setting up the LQ control problem with the cost function

$$J = \int_0^\infty Q_{z_1} z_1^2 + Q_{z_2} z_2^2 + Ru^2 + Q_I q^2\, dt. \qquad (46)$$

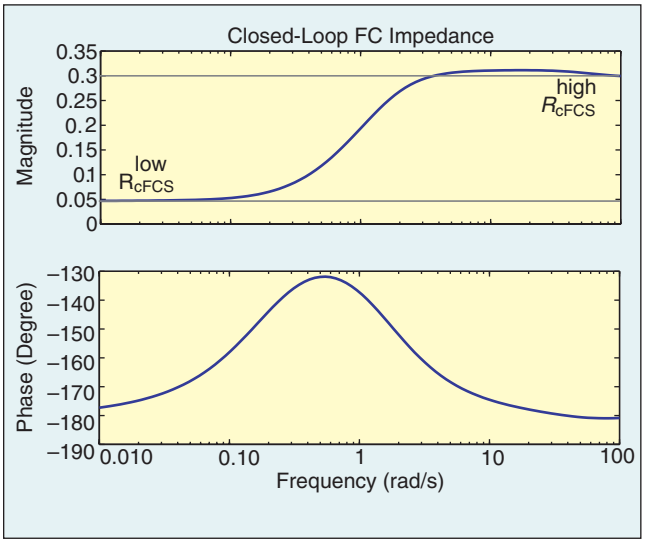

Figure 14. *Impedance of the controlled FC stack. Current signals with frequencies smaller than 0.1 rad/s cause six times lower impedance than currents with frequencies larger than 10 rad/s.*

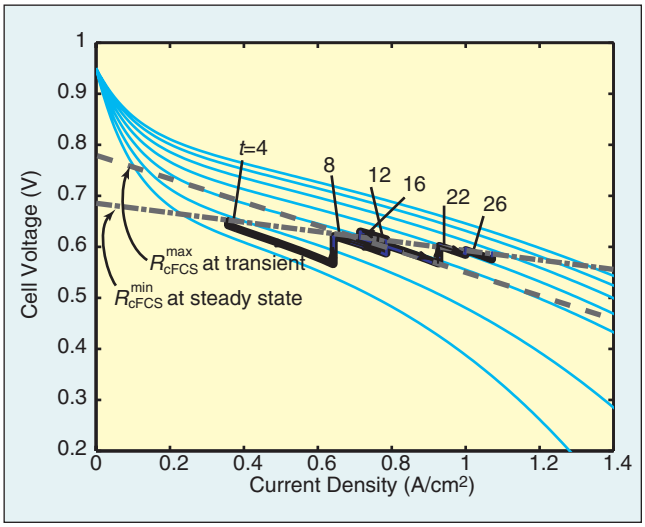

Figure 15. *Current-voltage trajectories in nonlinear simulation. These trajectories correspond to the nonlinear simulation of Figure 7.*

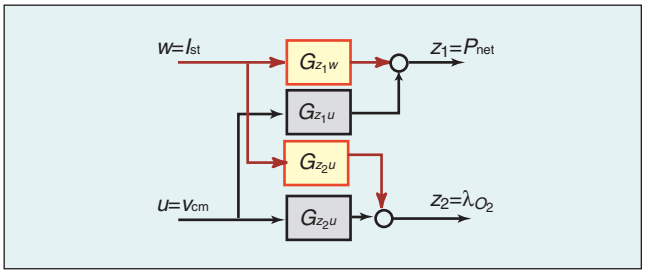

Figure 16. *Schematic showing the input-output coupling in the FCS air flow system. This coupling results in a tradeoff between fast oxygen (air) reactant supply that ensures long FCS life and transient FC net power response during rapid current (load) demands.*

Figure 18 shows the time responses of the linear model with different control gains based on different weightings in the cost function. The tradeoff between P_{net} and λ_{O_2} is evident during transient. In particular, controller design 4 (solid line) corresponds to the best power response but at the expense of slow recovery of the excess oxygen ratio. On the other hand, the fast recovery of excess oxygen ratio (dotted line) causes a net power lag of 0.2 s which might be viewed as undesirable.

The same results are shown in the frequency domain in Figure 19. The closer a curve is to zero, the better regulation is achieved. It can be seen that there is a severe tradeoff between the net power and the oxygen excess ratio in the frequency range between 0.7 rad/s and 20 rad/s. Inside this frequency range, when the magnitude of the error in

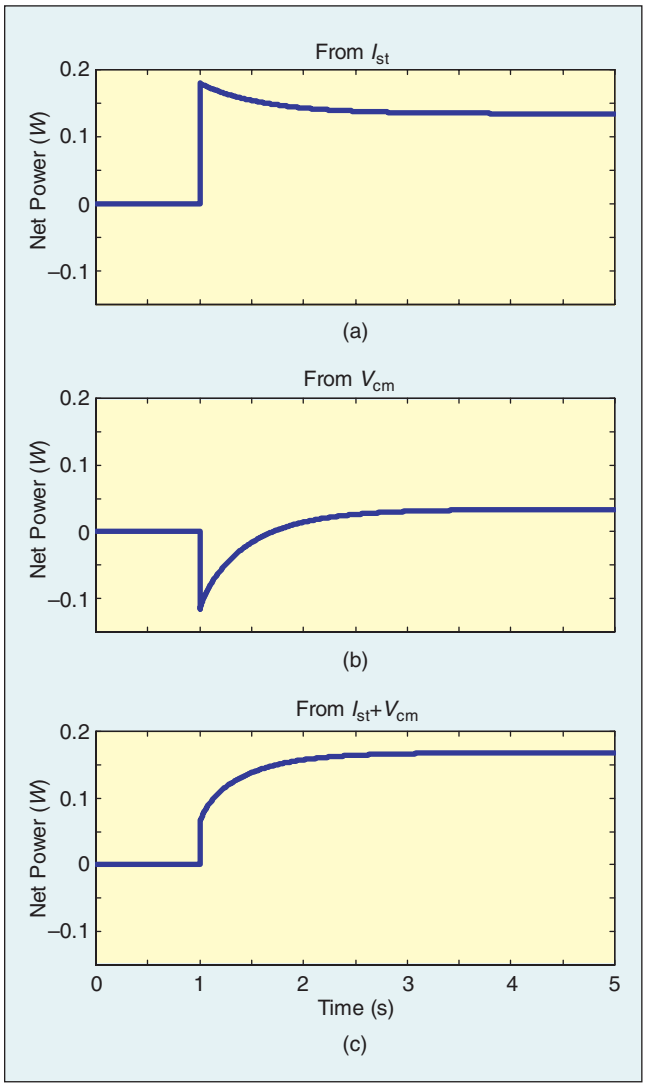

Figure 17. *Response of P_{net} to steps in (a) current I_{st}, (b) compressor voltage v_{cm}, and (c) coordinated I_{st} and v_{cm}. The compressor consumes a considerable fraction of the FC power during transients.*

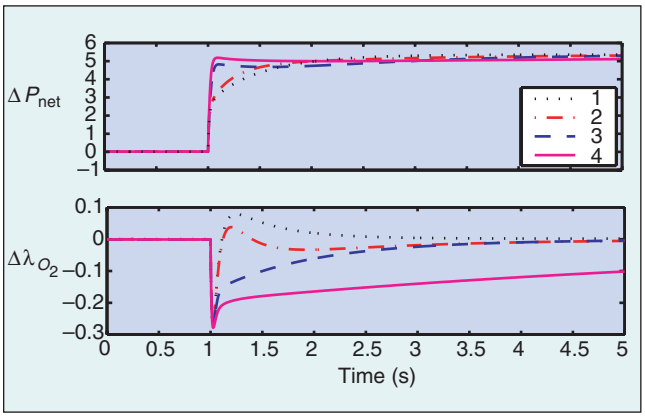

Figure 18. *Response of FCS linear system with different controllers. Linetypes 1, 2, 3 correspond to different feedback gains, whereas linetype 4 corresponds to the feedforward controller.*

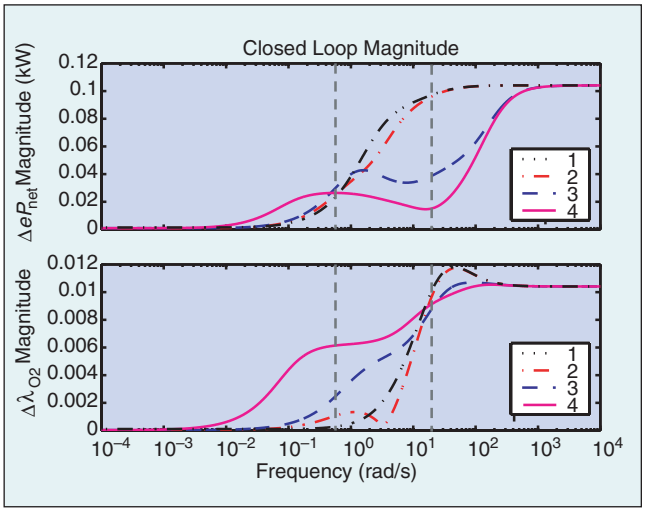

Figure 19. *Closed-loop frequency responses for different controllers. As in Figure 18, linetypes 1, 2, 3 correspond to different feedback gains, whereas linetype 4 corresponds to the feedforward controller.*

net power is pushed closer to zero, the magnitude of the error in the oxygen excess ratio "pops up" indicating worse λ_{O_2} regulation. To determine the best compromise between the two performance objectives, one needs to first establish a measure of how important the deviation in excess oxygen ratio is to the stack life.

One option for overcoming this tradeoff is to filter the current drawn from the stack and use an additional energy storage device such as battery or ultra-capacitor to supplement the system power during transient. Another option is to have an oxygen storage device placed near the entrance of the stack to provide an instant oxygen supply during rapid current changes. The required size of the energy or oxygen storage devices can be determined based on the frequencies associated with the tradeoff (Figures 9 and 19). The control analysis with the dynamic model of the FC system provides an important tool for identifying the required capacities of these storage devices.

Conclusion

In this article we analyzed and designed air flow controllers that protect the FC stack from oxygen starvation during step changes of current demand. The steady-state regulation of the oxygen excess ratio in the FCS cathode is achieved by assigning an integrator to the compressor flow. Linear observability techniques were employed to demonstrate improvements in transient oxygen regulation when the FCS voltage is included as a measurement for the feedback controller. Since this measurement has commonly been used for diagnostics and emergency shutdown logic, no extra cost is incurred. The FCS voltage signal contains high frequency information about the FC oxygen utilization, and thus, is a natural and valuable output for feedback.

We used linear optimal control design to identify the frequencies at which there is a severe tradeoff between the transient system net power performance and the stack starvation control. The limitation arises when the FCS system architecture dictates that all auxiliary equipment is powered directly from the FC with no secondary power sources. This plant configuration is preferred due to its simplicity, compactness, and low cost.

The FC current-voltage dynamic relationship is captured by the FCS impedance given the closed-loop air flow and perfect humidification and temperature regulation. More work is under way to characterize the FCS impedance for realistic humidification conditions [41]. We expect that the closed-loop FCS impedance will provide the basis for the systematic design of FC stack electronic components.

In the future, we will evaluate the air flow controller under uncertain conditions in the cathode air and membrane humidity. Moreover, we will evaluate our homogeneity assumption by studying the effect of spatial variations in the gas concentration across the flow field.

Acknowledgments

This work is funded by the National Science Foundation under contract NSF-CMS-0201332 and the Automotive Research Center (ARC) under U.S. Army contract DAAE07-98-3-0022. Jay Pukrushpan also acknowledges the Royal Thai government for his scholarship (1996–2002).

We are grateful to S. Staley, R. Bell, and W.-C. Yang of the Ford Motor Company for providing data on a vehicle FC system. We wish to thank C. Jacobson and S. Bortoff of the United Technology Research Center for their encouragement. Thanks are also due to J. Freudenberg and E. Gulari from the University of Michigan for their help and advice.

References

[1] C.F. Schoenbein, "The voltaic polarization of certain solid and fluid substances," *Philosoph. Mag.*, vol. 14, pp. 43–45, 1839.

[2] W.R. Grove, "A gaseous voltaic battery," *Philosoph. Mag.*, vol. 21, pp. 417–420, 1842.

[3] W.W. Jacques, "Electricity direct from coal," *Harper's Mag.*, vol. 94, pp. 144–150, 1896.

[4] K. Rajashekara, "Propulsion system strategies for fuel cell vehicles," SAE Paper 2000-01-0369.

[5] K. Jost, "Fuel-cell concepts and technology," *Automotive Eng. Int.*, pp. 173–185, Mar. 2000.

[6] F. Panik, "Fuel cells for vehicle applications in cars—Bringing the future closer," *J. Power Sources*, vol. 71, pp. 36–38, 1998.

[7] A.J. Appleby, "The electrochemical engine for vehicles," *Sci. Amer.*, pp. 74–79, July 1999.

[8] J.T. Pukrushpan, A.G. Stefanopoulou, S. Varigonda, L.M. Pedersen, S. Ghosh, and H. Peng, "Control of natural gas catalytic partial oxidation for hydrogen generation in fuel cell applications," in *Proc. 2003 American Control Conf.,* 2003, pp. 2030–2036.

[9] S. Varigonda, J.T. Pukrushpan, and A.G. Stefanopoulou, "Challenges in fuel cell power plant control: The role of system level dynamic models," in *Proc. AIChE Spring Meeting*, 2003.

[10] J.A. Adams, W.-C. Yang, K.A. Oglesby, and K.D. Osborne, "The development of Ford's P2000 fuel cell vehicle," SAE Paper 2000-01-1061.

[11] W.-C. Yang, B. Bates, N. Fletcher, and R. Pow, "Control challenges and methodologies in fuel cell vehicle development," SAE Paper 98C054.

[12] J.T. Pukrushpan, H. Peng, and A.G. Stefanopoulou, "Simulation and analysis of transient fuel cell system performance based on a dynamic reactant flow model," in *Proc. ASME Int. Mechanical Engineering Congress & Exposition,* 2002, pp. 1–12.

[13] J.T. Pukrushpan, H. Peng, and A.G. Stefanopoulou, "Modeling and analysis of fuel cell reactant flow for automotive applications," *ASME J. Dynam. Syst., Measure., Contr.*, to be published.

[14] L. Guzzella, "Control oriented modelling of fuel-cell based vehicles," presented at the NSF Workshop on the Integration of Modeling and Control for Automotive Systems, 1999.

[15] J. Padulles, G.W. Ault, C.A. Smith, and J.R. McDonald, "Fuel cell plant dynamic modelling for power systems simulation," in *Proc. 34th Universities Power Engineering Conf.*, 1999, vol. 34, pp. 21–25.

[16] S. Pischinger, C. Schönfelder, W. Bornscheuer, H. Kindl, and A. Wiartalla, "Integrated air supply and humidification concepts for fuel cell systems," *SAE Paper 2001-01-0233*.

[17] D.D. Boettner, G. Paganelli, Y.G. Guezennec, G. Rizzoni, and M.J. Moran, "On-board reforming effects on the performance of proton exchange membrane (PEM) fuel cell vehicles," *J. Energy Resources Technol., Transactions of the ASME*, vol. 124, no. 3, pp. 191–196, 2002.

[18] T.E. Springer, R. Rockward, T.A. Zawodzinski, and S. Gottesfeld, "Model for polymer electrolyte fuel cell operation on reformate feed," *J. Electrochem. Soc.*, vol. 148, no. 1, pp. A11–A23, 2001.

[19] M. Arcak, H. Gorgun, L.M. Pedersen, and S. Varigonda, "An adaptive observer design for fuel cell hydrogen estimation," in *Proc. 2003 American Control Conf.*, 2003. pp. 2037–2042.

[20] L.E. Lesster, "Fuel cell power electronics: Managing a variable-voltage DC source in a fixed-voltage ac world," *Fuel Cells Bull.*, vol. 2, no. 25, pp. 5–9, 2000.

[21] K. Ro and S. Rahman, "Control of grid-connected fuel cell plants for enhancement of power system stability," *Renewable Energy*, vol. 28, pp. 397–407, 2003.

[22] J. Freudenberg and R. Middleton, "Properties of single input, two output feedback systems," *Int. J. Contr.*, vol. 72, no. 16, pp. 1446–1465, 1999.

[23] J.T. Pukrushpan, "Modeling and control of fuel cell systems and fuel processors," Ph.D. dissertation, Univ. of Michigan, 2003.

[24] T.E. Springer, T.A. Zawodzinski, and S. Gottesfeld, "Polymer electrolyte fuel cell model," *J. Electrochem. Soc.*, vol. 138, no. 8, pp. 2334–2342, 1991.

[25] T.V. Nguyen and R.E. White, "A water and heat management model for proton-exchange-membrane fuel cells," *J. Electrochem. Soc.*, vol. 140, no. 8, pp. 2178–2186, 1993.

[26] B.A. Francis and W.M. Wonham, "The internal model principle of control theory," *Automatica*, vol. 12, no. 5, pp. 457–465, 1976.

[27] M.D. Di Benedetto and P. Lucibello, "Inversion of nonlinear time-varying systems," *IEEE Trans. Automat. Contr.*, vol. 38, no. 8, pp. 1259–1264, 1993.

[28] S. Devasia, D. Chen, and B. Paden, "Nonlinear inversion-based output tracking," *IEEE Trans. Automat. Contr.*, vol. 41, no. 7, pp. 930–942, 1996.

[29] S. Devasia, "Should model-based inverse inputs be used as feedforward under plant uncertainty?," *IEEE Trans. Automat. Contr.*, vol. 41, no. 11, pp. 1865–1871, 2002.

[30] R.S. Glass, "Sensor needs and requirements for fuel cells and CIDI/SIDI engines," Department of Energy, Lawrence Livermore National Lab., Tech. Rep., Apr. 2000.

[31] G.F. Franklin, J.D. Powell, and A. Emani-Naeini, *Feedback Control of Dynamic Systems.* New York: Addison-Wesley, 1994.

[32] J. Freudenberg, "A first graduate course in feedback control," Univ. of Michigan, EECS 565 coursepack, 2002.

[33] J. Sun and I. Kolmanovsky, "Robust reference governor for fuel cell oxygen starvation protection," IEEE 2004 American Control Conf., 2004, submitted.

[34] A. Vahidi, A.G. Stefanopoulou, and H. Peng, "Model predictive control for power management of a hybrid fuel cell system," IEEE 2004 American Control Conf., 2004, submitted.

[35] T. Kailath, *Linear Systems*. Englewood Cliffs, NJ: Prentice-Hall, 1980.

[36] C-T. Chen, *Linear System Theory and Design*. New York: Oxford Univ. Press, 1998.

[37] B.D.O. Anderson and J.B. Moore, *Optimal Control: Linear Quadratic Methods*. Englewood Cliffs, NJ: Prentice-Hall, 1989.

[38] J.C. Doyle and G. Stein, "Robustness with observers," *IEEE Trans. Automat. Contr.*, vol. AC-24, no. 4, pp. 607–611, 1979.

[39] V.A. Paganin, C.L.F. Oliveira, E.A. Ticianelli, T.E. Springer, and E.R. Gonzalez, "Modelistic interpretation of the impedance response of a polymer electrolyte fuel cell," *Electrochimica Acta*, vol. 43, no. 24, pp. 3761–3766, 1998.

[40] N. Wagner, W. Schnurnberger, B. Muller, and M. Lang, "Electrochemical impedance spectra of solid-oxide fuel cells and polymer membrane fuel cells," *Electrochimica Acta*, vol. 43, no. 24, pp. 3785–3793, 1998.

[41] P. Rodatz, "Dynamics of the polymer electrolyte fuel cell: Experiments and model-based analysis," Ph.D. dissertation, ETH-Zurich, 2004.

Jay T. Pukrushpan received his B. Eng. degree from Chulalongkorn University, Bangkok, Thailand, in 1995; M.S. degree from Michigan State University, East Lansing, in 1998; and Ph.D. degree from the University of Michigan, Ann Arbor, in 2003, in mechanical engineering. He is currently a faculty member at the Department of Mechanical Engineering, Kasetsart University, Bangkok, Thailand. His research interests include fuel cell system design, multivariable control system, hybrid systems, and fuel cell system and fuel processor controls.

Anna G. Stefanopoulou (annastef@umich.edu) obtained her diploma in 1991 from the National Technical University of Athens, Greece, in naval architecture and marine engineering and her Ph.D. in electrical angineering and computer science from the University of Michigan in 1996. She is an associate professor at the Mechanical Engineering Department at the University of Michigan. She was an assistant professor at the University of California, Santa Barbara (1998–2000), and a technical specialist at the Scientific Research Laboratories at Ford Motor Company (1996–1997). She received the 2003 outstanding paper award in the *IEEE Transactions on Control System Technology*, a 2002 Ralph Teetor SAE Educational Award, and a 1997 NSF CAREER Award. Her research interests are in control of internal combustion engines and fuel cell power systems. She can be contacted at the University of Michigan, Department of Mechanical Engineering, Room 2043 WE Lay Auto Lab, 1231 Beal Ave., Ann Arbor, MI 48109 USA.

Huei Peng received his Ph.D. in mechanical engineering from the University of California, Berkeley, in 1992. He is currently an associate professor in the Department of Mechanical Engineering and Director of the Automotive Engineering Program, University of Michigan, Ann Arbor. His research interests include adaptive control and optimal control, with emphasis on their applications to vehicular and transportation systems. He has served as chair of the ASME DSCD Transportation Panel from 1995 to 1997. Currently, he is an associate editor for the *IEEE/ASME Transactions on Mechatronics.* He received the National Science Foundation (NSF) Career award in 1998.